High-resolution scanning precession electron diffraction: alignment and spatial resolution

Jonathan S. Barnard, Duncan N. Johnstone, Paul A. Midgley

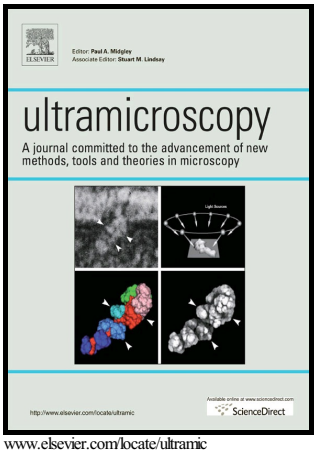

www.elsevier.com/locate/ultramic

PII: S0304-3991(16)30211-X
DOI: http://dx.doi.org/10.1016/j.ultramic.2016.12.018
Reference: ULTRAM12276

To appear in: *Ultramicroscopy*

Received date: 23 September 2016
Revised date: 23 December 2016
Accepted date: 24 December 2016

Cite this article as: Jonathan S. Barnard, Duncan N. Johnstone and Paul A Midgley, High-resolution scanning precession electron diffraction: alignment and spatial resolution, *Ultramicroscopy*, http://dx.doi.org/10.1016/j.ultramic.2016.12.018

High-resolution scanning precession electron diffraction: alignment and spatial resolution

Jonathan S. Barnard, Duncan N. Johnstone and Paul A. Midgley

Department of Materials Science & Metallurgy, University of Cambridge, 27 Charles Babbage Road, Cambridge, CB3 0FS, United Kingdom.

Abstract:

Methods are presented for aligning the pivot point of a precessing electron probe in the scanning transmission electron microscope (STEM) and for assessing the spatial resolution in scanning precession electron diffraction (SPED) experiments. The alignment procedure is performed entirely in diffraction mode, minimising probe wander within the bright-field (BF) convergent beam electron diffraction (CBED) disk and is used to obtain high spatial resolution SPED maps. Through analysis of the power spectra of virtual bright-field images extracted from the SPED data, the precession-induced blur was measured as a function of precession angle. At low precession angles, SPED spatial resolution was limited by electronic noise in the scan coils; whereas at high precession angles SPED spatial resolution was limited by tilt-induced two-fold astigmatism caused by the positive spherical aberration of the probe-forming lens.

Keywords: Electron diffraction, STEM, precession, strain, alignment

1. Introduction

The vast majority of technologically important materials, across myriad applications from electronics to structural engineering, are crystalline, or part crystalline, in nature. Many of the underlying physical, chemical and mechanical properties of these materials are dictated by the presence of crystal defects (e.g. grain boundaries, dislocations and strain) either by design or as a consequence of natural disorder. In either case, it is critically important to determine the crystallographic nature of the defects, often at the nanoscale, in order to understand the materials properties. As such, a technique is required to map changes in crystallography, with high spatial resolution and accuracy, which is adaptable to different materials and devices. Electron back-scatter diffraction (EBSD), performed in the scanning electron microscope, is extremely effective over length scales ranging from hundreds of micrometres down to several tens of nanometres [1], but the gap between ten

nanometres and the sub-nanometre scale remains. Scanning electron diffraction (SED) in the transmission electron microscope (TEM) is emerging as a strong contender to fill this gap. The technique involves rastering a nanometre-sized electron probe over an area of interest and recording the transmitted diffraction pattern at each probe position. The rise in popularity of SED has been driven by recent developments in scanning transmission electron microscopy (STEM) including: high brightness electron sources [2], flexible probe-forming electron optics [3], fast, high dynamic range pixelated detectors [4-6]; as well as the availability of computational power to process the large four-dimensional (4D) data-sets [7] obtained.

In many applications of SED, the geometry of each diffraction pattern is measured, almost always with an automated procedure. Such analysis can be improved by combining SED with precession electron diffraction (PED). In the PED method, known originally as the double-conical beam-rocking method [8], the incident electron probe is tilted away from the optic axis by the precession angle, ϕ, which is typically 0.5-3^{o}, and the tilt azimuth is rotated around the optic axis (Figure 1). For a crystal with a zone axis parallel to the optic axis, the tilted beam expands the zero-order Laue zone (ZOLZ) from a point to a circle (diameter equal to 2ϕ) and rotating the azimuth sweeps the ZOLZ circle around the optic axis, exciting many reflections temporarily as they pass through the Bragg condition (twice) for each complete rotation of the azimuth. By de-rocking the diffracted beams below the sample, the circular movement of the reflections, observed in the diffraction pattern, is arrested. The net effect is equivalent to precessing the sample around a stationary electron beam [8]. There are two significant advantages of precession: the number of reflections increases as the Ewald sphere rocks through many more reciprocal lattice points; and the thickness-dependence of the ensemble of reflections appears to be slower, i.e. the reflections are ‘kinematic-like’ [9-11]. Together, this has made zone-axis PED patterns particularly amenable for structure solution problems [12-14].

Scanning precession electron diffraction (SPED) involves rastering a precessing probe over an area of interest and recording a PED pattern at each probe position. This has been implemented on a number of microscopes and has proved advantageous for orientation imaging [15-17], phase identification [18], strain mapping [19-22], and three-dimensional interphase crystallography [23]. Perhaps most striking is the improvement in precision for strain measurement and mapping, which is of key importance in the semiconductor industry where strain is introduced to increase carrier mobility [24]. The improvement in strain measurement in SPED is attributable to: i) more reflections being recorded in each PED pattern; ii) the presence of higher order reflections increasing the sensitivity to small strains; iii) the position of each reflection being more easily located, because each PED reflection is a uniformly filled convergent beam electron diffraction (CBED) disk [25]. Finally, it is noted that, with the addition of an EDX spectrometer, the fidelity of composition measurement is improved because unwanted channelling conditions are averaged out by the beam rocking action [26].

For precession-enabled techniques (PED and SPED) the alignment procedure must accommodate the need to bring the precession pivot point into coincidence with the sample. If the STEM is fitted with an aberration corrector in the imaging (post-specimen) lens [19-22], then the image of the probe on the viewing screen is a reasonably accurate representation of the probe at the sample. Minimisation of probe wander on the viewing screen, with the sample in focus, is then a sufficient condition for achieving the correct pivot point for all but the highest precession angles. For non-image-corrected instruments, spherical aberration in the imaging lens and small misalignments between the pre-field and post-field objective lens pole pieces leads to significant misrepresentation of the probe position and shape on the viewing screen [27]. Aligning the pivot point in imaging mode can be successful if the probe movement relative to the sample is minimized [28]. However, it is emerging that the shadow image in a bright-field (BF) CBED disk, rather than the image of the probe, is a more appropriate representation for aligning the pivot point accurately [28]. This paper shows that the pivot point can be aligned entirely in diffraction mode; by using the shadow image in the BF-CBED

disk. An explicit alignment procedure is provided and applied to obtain high spatial resolution SPED data sets. Physical limitations imposed by electronic noise in the scan coils and aberrations in the probe forming lens are also considered in detail.

2. Materials

All data presented here were acquired using an FEI/Philips CM300F TEM operated at 300 kV with a Schottky thermionic source and working in microprobe mode. Both scanning and precession were enabled through a NanoMEGAS Digistar system hardwired into the microscope scan control boards. The system was controlled through the NanoMEGAS ASTAR software package using a Stingray fast capture CCD camera to capture the diffraction patterns as seen on the small viewing screen of the microscope.

The proposed alignment procedure (Figure 3) was demonstrated with a Ted Pella test sample (product number 673) comprising a carbon replica of a crossed diffraction grating (500 nm pitch), shadow-coated with gold-palladium and decorated with 262 nm diameter latex spheres. The probe illumination semi-angle (α) and the precession angle (ϕ) were measured to be 3.35 mrad and 16.6 mrad respectively. The camera length was 850 mm.

The spatial resolution in SPED was assessed (Figure 4) using an Agar Scientific combined test specimen (Product number S142), comprising a holey carbon film (thickness, $t = 20$ nm) decorated with a uniform distribution of gold particles approximately 10 nm in diameter. SPED data comprising diffraction patterns with 144×144 pixels and 8 bits per pixel were acquired with a spatial sampling of 1.9 nm/pixel and 256×256 data points (486 nm square). Precession angles (ϕ) between 1.4 mrad and 41 mrad (calibrated in-situ using polycrystalline gold ring patterns) were used with alignment performed as described in this work and at a precession frequency of 100 Hz. All data were acquired with: an illumination semi-angle, $\alpha = 0.91$ mrad; a probe current of 0.5 pA; a camera length of 850

mm; and a 10 ms exposure time such that diffraction patterns recorded on the Stingray camera were not saturated.

3. Methods

3.1 Aligning a precessing probe

Aligning a precessing probe should begin with the microscope well aligned for conventional TEM imaging in microprobe mode. Particular attention should be paid to the conventional pivot point alignment and current centring of the objective lens. The sample should be set to the eucentric height with the objective lens optimally excited and the image in focus. The procedure described here then gives a route to align the double-rocking beam of a precessing electron probe.

The principles of aligning a precessing electron probe using the shadow image are illustrated in Figure 2. The most general condition occurs when the probe focal plane, C, pivot point plane, P, and the specimen plane, S, are at different heights (Figure 2(a)). As the probe moves around the sample, during precession, the shadow image of the specimen describes a circular path within the BF-CBED disk. Two snapshots at opposite positions on the precession cone are shown to illustrate this (Figure 2(a)). As the precession pivot point alignment is improved, the pivot point, P, moves closer to the specimen plane, S, and the circular movement of the shadow image within the BF-CBED disk is reduced at the same angular magnification (Figure 2(b)). Only when the pivot point plane, P, coincides with the specimen plane, S, does the shadow image of the specimen no longer move within the bright-field disk (Figure 2(c)). The incident angle continues to change so, if the sample diffracts, the static image will twinkle. Finally, when the probe focal plane, C, is moved into coincidence with the pivot point, P, and the specimen plane, S, the bright-field disk becomes featureless and any change in intensity is due to the diffraction condition alone (Figure 2(d)).

In practice, alignment (see Figure 3) involves defocusing the condenser lens to obtain a high contrast shadow image, over a sufficiently wide field of view, within the BF disk (step 1). Successful pivot-

point alignment of the precessing probe (step 2) requires that the de-rocking, below the specimen, is also aligned to keep the BF disk stationary. Since the de-rocking is contingent on the position of the pivot point plane, iterative refinement of the pivot-point and de-rocking is necessary (steps 3 and 4). The spatial accuracy of the pivot point alignment is only as good as the angular resolution and the angular magnification within the BF disk. Therefore, the defocus is reduced, typically by a factor of two (step 5), several times, to increase the angular magnification and reduce the pivot point error. When no further improvement in the pivot point can be accomplished by the pivot point adjustment alone, dynamic compensation is applied (step 6). Dynamic compensation modulates the beam shift coils, over the precession cycle, to null probe shifts caused by non-round aberrations in the probe forming lens [29]. Like the pivot point adjustment, the dynamic compensation is refined by reducing motion of the shadow image within the BF disk during precession[1]. The non-precessed shadow image is depicted for comparison in Figure 3 and any blur must be related to residual pivot point error or electronic noise in the scan coils. The alignment is terminated when no further sharpening is seen. The probe is then refocused using the condenser lens and a smaller illumination aperture is inserted (step 7). In summary, the alignment (Figure 3) is described by the following steps:

1. Insert a large illumination aperture and over-focus the electron probe using the condenser lens (see Note 1);
2. Find a region with highly visible features and activate precession at both the precession angle (ϕ) and precession frequency to be used (see Note 2);
3. Obtain a static BF-CBED disk using the de-rocking adjustment (Image Upper and Lower deflectors, figure 1);
4. Minimize motion of the shadow image within the BF disk by adjusting the pivot point (Beam Upper & Lower deflectors, figure 1);

[1] Note that reducing motion of the shadow image within the BF-CBED disk is equivalent to sharpening the time averaged shadow image obtained by integrating on the detector over a time longer than one precession cycle. This sharpening interpretation can be particularly useful for the final refinement and is seen in Figure 3.

5. Reduce the defocus by a factor of two and repeat steps 3 and 4 until no further improvement is seen;
6. Apply dynamic compensation to further reduce motion of the shadow image within the BF-CBED disk;
7. Refocus the probe using the condenser lens and insert a smaller illumination aperture (see Note 3).

Three further points are worth making. First, the initial gross errors in both the pivot point and de-rocking for precession angles beyond ca. 20 mrad (> 1°), make correction with steps 2, 3 and 4 difficult. By starting with a lower precession angle and finding the correct pivot point and de-rocking settings there and then increasing ϕ, in a stepwise fashion, the correct pivot point and de-rocking settings can be found, i.e. steps 2, 3 and 4, can be iteratively refined with an increasing precession angle. Second, when moving the sample from the alignment region to the region of interest (ROI), the height of the new region has to be set carefully, as a height deviation Δz from the pivot point plane will resultant in conic blur of approximately $\phi\Delta z$. To achieve this, having set the pivot point plane at the alignment region, precession can be switched off and the probe focussed to Gaussian focus, the specimen is then moved to the ROI and the height adjusted to give the same Gaussian focus conditions as before. Precession can be turned back on and the condenser lens underfocused by $2C_{30}\phi^2$, where C_{30} is the spherical aberration coefficient of the probe forming lens, (see Discussion & Figure 6) before starting the SPED scan over the ROI. Finally, it is noteworthy that the specimen height is typically not changed significantly in this procedure allowing a position close to eucentric height to be maintained, which is advantageous for scanning precession electron tomography [23] experiments.

3.2 Note 1. Why align with positive defocus (overfocus)?

In the geometric ray framework, a ray passing through a point in the illumination aperture, $\vec{k} = (k_x, k_y)$, passes through the point, $\vec{r} = (x, y)$, in the conjugate Gaussian imaging plane, according to [30-32]:

$$(x, y) = \frac{1}{2\pi}\left(\frac{\partial \chi}{\partial k_x}, \frac{\partial \chi}{\partial k_y}\right) \quad (1)$$

where $\chi(k_x, k_y)$ is the aberration function of the probe-forming lens [33], i.e. the Gaussian image plane coordinates are gradient mappings of the aberration function in Fraunhofer diffraction [30]. For an aberration free probe-forming lens, only the defocus term, $\chi(\vec{k}) = \pi C_{10} \lambda k^2$, contributes to the aberration function. When the probe is underfocused ($C_{10} < 0$) or overfocused ($C_{10} > 0$) there is a linear, one-to-one correspondence between a point in the diffraction disk and a point on the sample within the illuminated area of the probe. Either condition works for aligning a precessing probe.

For a microscope with positive spherical aberration (C_{30}) in the probe forming lens, the one-to-one relationship is maintained *only with a positive defocus* (overfocus). If underfocus is used, the one-to-one correspondence is lost over a range of defocus, resulting in strong warping within the shadow image due to natural focusing as the curvature of the aberration function disappears at certain regions within the illuminated cone [30-32]. This makes pivot point correction difficult. An additional, practical, benefit of using the overfocus condition is the slight widening of the illumination aperture, rendering a wider field of view.

3.3 Note 2. Why not align at a lower precession frequency?

For a modern digitally controlled electron microscope the beam tilt and shift are actuated by reference voltages fed to pre-amplifiers and current amplifiers, which drive the deflector coils of the scan and de-rocking system [29]. The Lorentz force that deflects the electron beam is determined by

the current flow in the coil, not the voltage across it. Each deflector coil is an inductor, with inductance, L_{coil}, connected in series to a foot resistor, R_{foot}, with a phase lag between current and voltage that is determined by the total impedance of the deflector coil and foot resistor circuit [34]. In effect, each of the eight scan coils (Upper and Lower, Beam and Image, X and Y) is an independent *LCR* circuit with a phase lag equal to: $arctan\left(\omega L_{coil}/\left(R_{coil}+R_{foot}\right)\right)$, when internal coil resistance, R_{coil}, is accounted for and assuming that there is no stray capacitance (for very high precession & scan speeds, e.g. >1 kHz, this would also need to be accounted for). At typical precession frequencies (e.g. 100 Hz) the phase lag may become substantial, causing significant mis-registration of both the BF-CBED disk (during the de-rocking) and the shadow image within it (pivot point) throughout the precession cycle. Further, slight differences in impedance between the deflectors cause increasing discrepancy as the precession frequency is raised. Therefore, aligning the precession pivot point using a lower precession frequency (for ease or convenience) implies that, when a higher frequency is used for the scan, the pivot point and de-rocking alignments will be wrong. This can be easily observed by watching the shadow image change as the precession frequency is varied – there is a strong linear response to the frequency change, which is correctable through pivot point and de-rocking *phase* adjustments.

3.4 Note 3. Why change to a smaller illumination aperture?

Together with the lattice parameter of the material under examination, the illumination aperture determines the extent of reflection overlap in the PED pattern. Automated reflection identification generally requires non-overlapping CBED disks, i.e. smaller illumination apertures. The size of the precessing probe is also determined by the aperture size (see Discussion below and Equation 4) and smaller apertures generally improve spatial resolution of SPED data sets.

In practical terms, the illumination aperture is typically changed in imaging mode. However, it is advantageous to operate only in diffraction mode to avoid any effects of hysteresis in the intermediate lenses. To maintain this advantage, the illumination aperture can be changed in diffraction mode and positioned with reasonable accuracy by marking the position of the BF-CBED disk centre with the larger illumination aperture aligned and then inserting the smaller aperture and adjusting its position to return the BF-CBED disk to the same position.

3.5 Measuring spatial resolution in SPED

STEM probe size measurement is typically performed using a grating or nanostructure with a well-defined lateral size [35]. In SPED, the same approach is desirable, but the (usual) need to maintain non-overlapping disks in the SPED diffraction patterns means lattice fringes will not be visible. Instead, each 4D SPED dataset was processed using the HyperSpy Python library [7] to extract 32-bit virtual bright-field images (VBFs) by mapping, as a function of probe position, the integrated intensity within a circular region centred on the BF disk of each diffraction pattern. The integration disk was slightly larger than the convergence semi-angle with a disk radius of 1.2 mrad.

Precession-induced blur, i.e. spatial resolution *loss*, was determined by measuring the effective damping envelope, in the Fourier domain, of the *rotationally averaged* VBF power spectra at low spatial frequencies ($k < 0.2$ nm^{-1}). If the effect of precession-induced blur can be modelled as a Gaussian blur (width, d) of an unprecessed VBF image, then, in the Fourier domain, the power spectrum of the precessed VBF, $\rho(k|\phi)$, is equal to the unprecessed VBF power spectrum, $\rho(k|0)$, multiplied by a Gaussian damping envelope, $exp(-4\pi^2 d^2 k^2)$. Therefore, taking the logarithm of the ratio of the power spectra, $\rho\,(k|\phi)/\rho\,(k|0)$, should yield a parabolic variation in the low$-k$

domain[2]. A least-squares fitting algorithm was used to find the parabolae that matched the log-power-spectra-ratio (LPSR),

$$L(k) = \log_{10}\left(\frac{\rho(k|\phi)}{\rho(k|0)}\right) \quad (2)$$

in the low$-k$ domain, using one or two parameter fits. In the one-parameter fit, $L(k) = -4\pi^2 d^2 k^2 \log_{10} e$, i.e. proportional to the square of the Gaussian blur, d. The single-parameter fit implicitly assumed that the total intensity in precessed and unprecessed VBFs were the same. In the two-parameter fit, i.e. $L(k) = A - 4\pi^2 d^2 k^2 \log_{10} e$, where A is a (fitting) constant, considers the possibility that total VBF intensity is different. The blur coefficients, d, were used as a proxy for precession probe size.

4. Results

Figure 4 shows the VBFs and their power spectra for a range of precession angles. As expected, the sharpest images were without precession ("$\phi = 0$ mrad") and the gold particles were easy to discern with sharp edges. Darker-than-average contrast amongst some particles suggested they were diffracting strongly. Indeed, their corresponding diffraction patterns showed several CBED disks excited. As the precession angle was increased, the blur in the VBF was modest, e.g. 3.4 and 13.5 mrad, and faint blurring could be seen at the edge of the gold islands. No stretching of the islands was apparent, suggesting that contrast transfer by the SPED probe was isotropic.

Increasing the precession angle beyond approximately 20 mrad led to a rapid increase in the VBF blur. During the alignment it was more difficult to keep the islands sharp within the shadow image and significantly larger features, such as holes in the carbon film and clusters of gold particles, were needed to find the correct pivot point. Above 35 mrad (ca. 2°) precession angle the VBF images

[2] This argument holds even if the precessed and unprecessed images are not of the same area. The only requirement is that the statistical properties of the gold-on-carbon films were the same, i.e. island size, spatial homogeneity. All indications were that this was indeed the case.

demonstrated some streakiness, which was evident within the power spectra as lines of zero-visibility (Figure 4); this suggested some anisotropy in the transfer of contrast.

Figure 5(a) shows the LPSRs for low, medium and high precession angles, with their respective parabolic fits to the low$-k$ domain. The domain over which the parabolic fit was appropriate became narrower with increasing precession angle. The prominent rise in the LPSR for the 13.5 (33.7) mrad curves in the domains $k > 0.15$ ($k > 0.10$) nm^{-1}, was due to algebraic nature of the LPSR. Rewriting the LPSR,

$$L(k) = \log_{10} \rho(k|\phi) - \log_{10} \rho(k|0) \quad (3)$$

shows that the high$-k$ domain of $L(k)$ is dominated by the large (negative) values of the unprecessed VBF image, i.e. there is more high$-k$ structure in the unprecessed VBF power spectrum. This creates a strong negative dip in the LPSR. However, as $k \to \infty$, the power spectra of both VBFs tends to the *same frequency-independent noise floor*, so that their ratio, the LPSR, tends to $\log_{10} 1 = 0$. Simply interpreted, the rise is due to the precessed VBF power spectrum hitting the frequency-independent noise floor *before* the unprecessed VBF power spectrum. Thus, the spatial-frequency domain over which the parabolic approximation is valid continues to shrink for increasing precession angle.

Figure 5(b) shows the Gaussian blur measured for each precession angle LPSR function, plotted against the measured precession angle, for both the 1-parameter and 2-parameter parabolic fitting functions. Both 1-parameter and 2-parameter models show the same slow increase in the blur, which, with a least squares fit, scales as $\phi^{0.4}$ for precession angles below 15 mrad. Above 15 mrad (ca. 1^{o}), the resolution worsens faster, scaling as $\phi^{1.7}$ and $\phi^{1.6}$ for the 1-parameter and 2-parameter fits respectively. Asymptotically, both curves appear to approach the Vincent-Midgley expression, $d = 4C_{30}\phi^2\alpha$, in the high-ϕ limit, which is shown for comparison [8]. Both the 1-parameter and 2-parameter blur curves show that the VBF images for a precessed electron probe

can be equated to an unprecessed VBF with Gaussian blur of $d < 2$ nm for precession angles less than about 15 mrad (ca. 1°).

5. Discussion

The shadow image, or Ronchigram, is an in-line hologram of the sample [36, 37]. Its sensitivity to the phase distribution of the probe-sample interaction has made it one of the most important signals for STEM alignment, both before [38,39] and after the introduction of aberration correction [40-43]. As pointed out by Liao & Marks, it is the probe-forming lens that determines the precession probe shape at the sample and they acknowledged the point that aligning precession may have to be done in STEM mode [27]. Our results support this assertion - aligning the precessing probe with the shadow image is the most appropriate method. Performing the alignment entirely in diffraction mode also mitigates the problem of intermediate lens hysteresis caused by switching between diffraction and imaging modes. However, aligning precession with the shadow image is not without problems and there are three.

First, a large illuminating aperture (in the condenser lenses) is necessary for the alignment, which has to be changed to a smaller aperture for the experiment. This has two consequences: i) If one, or both apertures are dirty, the precessing probe acquires an additional aberration that stays constant throughout the precession cycle. As with regular STEM, this can be corrected by adjusting the condenser stigmators; ii) If the small aperture centre does not sit precisely on the precession circle, the probe acquires a sinusoidal probe displacement and aberration. This is perhaps the biggest weakness of our method.

The second problem is the need to find a prominent feature to align the precessing probe, especially with the relatively large (ca. 100 µm) defocus used at the start of the alignment process (Figure 3). We have found that small (ca. 10 nm) features work well for modest precession angles, up to about 20 mrad (ca. 1°) with larger (ca. 100 nm) features necessary for precession angles above this.

Corners of specimens work well too – two sharp edges provide reliable information about the probe wander in the orthogonal directions - especially for the dynamic compensation at the end of the alignment procedure (step 6, figure 3). However, the need to find appropriate features for alignment is a common part of much electron microscopy and typically a suitable feature can be found or contrived.

Third, shadow image contrast in the CBED disk is low for microscopes with W-filament and LaB_6 thermionic emitters, because the overall shadow image is an incoherent superposition of individual shadow images from points within the (extended) crossover sitting above the sample. Visibility is improved by reducing the spot size, but at the expense of probe current. In contrast small, coherent sources such as a Schottky thermionic emitter or cold field emitter afford significantly greater precession probe currents (>1 pA). Users of SPED systems fitted to older microscopes may, therefore, find the shadow image alignment challenging.

Measurement of the probe size by estimating the damping envelope of the power spectra associated with VBF images appears to give reasonable results. The ca. 10 nm gold particles on an approximately 20 nm carbon film provided a sufficiently thin test sample so that the conical blur of the precessing probe, ϕt (thickness, t), was small, typically less than 1 nm for all the precession angles used. The isotropic nature of the sample facilitated the rotational averaging of the power spectra too. Further, the substantial difference in scattering power between the gold and carbon ensured that we had a stable, radiation-hard sample with high contrast. It should be noted that it is critical to form the VBF images in a manner that preserves bit-depth, without rescaling, in the same way for all VBFs in order to make a proper like-for-like comparison, which was possible with HyperSpy. This is noteworthy because it is not the behaviour of some commercial solutions.

The precession angle dependence of the resolution degradation can be explained as follows. At low precession angles, the $\phi^{0.4}$ dependence is close to $\sqrt{\phi}$, which suggests not an aberration, but noise in the scan electronics. This argument is predicated on two suppositions. First the angular

displacement of the electron beam by a deflector coil is proportional to the current flowing through it. Second, noise in the deflector coil is primarily shot noise, which increases in proportion to the square root of *total* current flowing through it [44]. Therefore, the (shot) noise in each deflector coil, even when the probe is stationary at a pixel point, is related to the total current, $I_{tilt}(t) + I_{shift}$, not just the shift signal. Effectively, the probe shift signal is superposed on the same noisy electronic channel that the (precession) tilt signal passes. One possible method to mitigate this would be to have separate deflector coils for the (probe) shift and (precession) tilt actions. It has to be noted that, since the CM series of instruments used in this work, considerable improvement in the electronic noise in the scan system of subsequent microscope platforms has been achieved.

At high precession angles the $\phi^{1.7}$ dependence seen (Figure 5) is close to the ϕ^2 dependence for the disk of least confusion, as suggested by Vincent & Midgley [8]. If we had pushed the precession angle higher, then the curve in Figure 5(b) would almost certainly have steepened. Thus, by using the shadow image alignment method, we appear to be reaching the limit in spatial resolution dictated by spherical aberration of the probe forming lens ($C_{30} = 1.2$ mm) and the tilt-induced two-fold stigmatism, $C_{12}^{eff} = 2C_{30}\phi^2$, of the precessing probe.

Finally, it is worth pointing out that the expression for the disk of least confusion, $d = 4C_{30}\phi^2\alpha$, posed originally by Vincent & Midgley is slightly pessimistic [8]. Figure 6 shows the full wave-optical structure of the inclined probe at one instantaneous azimuth in the precession cycle, for two different illumination aperture sizes. For the α=3 mrad aperture, the probe is an ellipse at the Gaussian imaging plane ($z = 0$) with a small amount of coma (magnitude, $C_{21}^{eff} = 6C_{30}\phi$), which makes the probe slightly brighter on one side. Above the Gaussian imaging plane, i.e. the overfocusing condition, two line foci are seen and separated in height by a distance equal to the tilt-induced two-fold stigmatism, $C_{12}^{eff} = 2C_{30}\phi^2$ (this is the definition of 2-fold stigmatism). Detail of the probe at height, $z = 2C_{30}\phi^2$, i.e. midway between the line foci, shows that the 3 mrad probe is comprised of four fold caustics decorated with Airy fringes [30]. The top-bottom pair are azimuthal

fold caustics that coalesce at height, $z = C_{30}\phi^2$, to form one line-focus. The left-right pair are radial fold caustics that coalesce at height, $z = 3C_{30}\phi^2$, to form the other (orthogonal) line focus. Between the two, the probe is underfocused in one direction (azimuthally) and overfocused in the other (radially). The probe is also at its most compact size, having a size $2C_{30}\phi^2\alpha$ according to the geometric ray model, i.e. half that of the Vincent-Midgley expression. A full wave-optical assessment shows that the probe is slightly smaller still, $r_{80} = 0.89C_{30}\phi^2\alpha$ (80% probe intensity), compared to the Vincent-Midgley expression, $4C_{30}\phi^2\alpha$ (see Appendix).

By balancing the tilt-induced two-fold astigmatism against the diffraction limit, we have shown previously that the optimum illumination aperture semi-angle is [45]:

$$\alpha_{opt}(\phi) = 0.55\sqrt{\frac{\lambda}{C_{30}\phi^2}} \sim \frac{1}{\phi} \quad (4)$$

For a given precession angle, ϕ, and wavelength, λ. This yields an optimum probe size of [45]:

$$d_{opt}(\phi) = 2.19\sqrt{\lambda C_{30}\phi^2} \sim \phi \quad (5)$$

I.e. if we had optimized the illumination aperture for each precession angle, then our precession-induced blur would have increased more slowly than we see in Figure 5(b) where we kept a fixed illumination angle. This strategy is possible with STEMs equipped with three condenser lenses [3]. The prospect of reaching sub-nanometre-resolution SPED, however, resides entirely within the confines of aberration-corrected electron optics for the probe-forming lens [45,46].

6. Conclusion

We have demonstrated that, by using the shadow image, or Ronchigram, to align a precessing probe, at its operating frequency, it is possible to achieve high-resolution scanning precession electron diffraction (SPED) maps. One method for assessing the size and shape of the SPED probe was suggested. We showed that probe was limited by electronic noise in the scan coils at low

precession angles and tilt-induced two-fold stigmatism, caused by the positive spherical-aberration of the probe forming lens, at high precession angles.

Acknowledgements

The research leading to the results presented in this work received funding from the European Research Council under the European Union's Seventh Framework Programme (FP7/2007–2013)/ERC grant agreement 291522–3DIMAGE) and the European Union Seventh Framework Programme under Grant Agreement 312483-ESTEEM2 (Integrated Infrastructure Initiative – I3). The authors also acknowledge support from the University of Cambridge through the Cambridge Home and EU Scholarship Scheme and the Cambridge NanoDTC. Finally, we acknowledge the two Reviewers for their valuable comments during the reviewing process.

Appendix A

The probe size midway between line foci was measured using simulated wave-optical calculations calculated in IDL using a fast Fourier transform (FFT) [47]. The defocused probe was calculated using a defocus term equal to $C_{10} = -2C_{30}\phi^2$ (the precession angle, ϕ, was fixed at 35 mrad) in the aberration function and various circular illumination apertures applied to low-pass the spatial frequencies, $0.1 \leq \alpha \leq 4.1$ mrad, in the probe wave-function, $\psi_{probe}(\vec{k})$ prior to the FFT. The results of the probe intensity $\left|\psi_{probe}(\vec{r})\right|^2$ are depicted in Figure A1(a) for one instantaneous precession azimuth. Because the probe rotates around the optic axis (assuming the probe is centred on the optic axis) the *radially averaged* probe is pertinent to the spatial resolution of the SPED experiment. The integrated radial probe profile is depicted in Figure A1(b) with two lines, corresponding to the 50% (red) and 80% (green) probe intensity thresholds. Least-squares-fits of these intensity thresholds correspond to:

$$r_{50} = 0.67C_{30}\phi^2\alpha \qquad \text{and} \qquad r_{80} = 0.89C_{30}\phi^2\alpha$$

Which compares to the Vincent-Midgley expression, $4C_{30}\phi^2\alpha$, which is the width of the two line-foci sitting above and below this focus setting [8].

References

[1] A.J. Wilkinson and T.B. Britton, *Strains, planes, and EBSD in Materials Science* (2012), Materials Today **15** (9) 366-376. Doi: 10.1016/S1369-7021(12)70163-3

[2] L.W. Swanson and G.A. Schwind, *Review of the ZrO/W Schottky Cathode* (2008) Chapter 1, in Handbook of Charged Particle Optics (2nd Ed), J. Orloff (Ed), CRC Press, Taylor & Francis, New York.

[3] F. Yi, P. Tiejmeijer and P.M. Voyles, *Flexible formation of coherent probes on an aberration-corrected STEM with three condensers* (2010) J. El. Microscopy **59** S15-21. Doi: 10.1093/jmirco/dfq052

[4] A. Mac Raighne, G.V. Fernandez, D. Maneuski, D. McGrouther and V. O'Shea, *Medipix2 as a highly flexible scanning/imaging detector for transmission electron microscopy* (2011) Journal of Instrumentation **6** C01047

[5] K. Müller, H. Ryll, I. Ordavo, S. Ihle, L. Strüder, K. Volz, J. Zweck, H. Soltau and A. Rosenauer, *Scanning transmission electron microscopy strain measurement from millisecond frames of a direct electron charge coupled device* (2012) Applied Physics Letters **101** 212110. Doi: 10.1063/1.4767655

[6] M.W. Tate, P. Purohit, D. Chamberlain, K.X. Nguyen, R. Hovden, C.S. Chang, P. Deb, E. Turgut, J.T. Heron, D.G. Schlom, D.C. Ralph, G.D. Fuchs, K.S. Shanks, H.T. Philipp, D.A. Muller and S.M. Gruner, *High dynamic range pixel array detector for scanning transmission electron microscopy* (2016) Microscopy & Microanalysis **22** 237-249. Doi: 10.1017/S1431927615015664

[7] F. de la Peña *et al* (2016), hyperspy: HyperSpy 1.0.1. Zenodo. Doi: 10.5281/zenodo.58841

[8] R. Vincent and P. A. Midgley*, Double conical beam-rocking system for measurement of integrated electron diffraction intensities*, Ultramicroscopy 53 (1994) 271-282

[9] W. Sinkler and L.D. Marks, *Characteristics of precession electron diffraction intensities from dynamical simulations* (2010) Z. Kristallogr. **225** 47-55

[10] T.A. White, A.S. Eggeman and P.A. Midgley, *Is precession electron diffraction kinematical? Part I: "Phase scrambling" multislice simulations* (2010) Ultramicroscopy **110** 763-770

[11] A.S. Eggeman, T.A. White and P.A. Midgley, *Is precession electron diffraction kinematical? Part II: A practical method to determine the optimum precession angle* (2010) Ultramicroscopy **110** 771-777

[12] P.A. Midgley, M.E. Sleight and R. Vincent, *The structure of a metastable Au-Sn phase determined by convergent beam electron diffraction* (1996) J. Sol. St. Chem. **124** (1) 132-142.

[13] W. Sinkler, L.D. Marks, D.D. Edwards, T.O. Mason, K.R. Poeppelmeier, Z. Hu and J.D. Jorgensen, *Determination of oxygen atomic positions in a Ga-In-Sn-O ceramic using direct methods and electron diffraction* (1998) J. Sol. St. Chem. **136** 145-149.

[14] J. Gjønnes, V. Hansen, B.S. Berg, P. Runde, Y.F. Cheng, K. Gjønnes, D.L. Dorset and C.J. Gilmore, *Structure model for the phase Al_mFe derived from three-dimensional electron diffraction intensity*

data collected by the precession technique. Comparison with convergent beam diffraction (1998) Acta. Crys. A**54** 309-319.

[15] E.F. Rauch, J. Portillo, S. Nicolopoulos, D. Bultreys, S. Rouvimov & P. Moeck, *Automated nanocrystal orientation and phase mapping in the transmission electron microscope on the basis of precession electron diffraction* (2010) Z. Kristallogr. **225** 103-109. Doi: 10.1524/zkri.2010.1205

[16] A. Kobler, A. Kashiwar, H.Hahn and C. Kübel, *Combination of in-situ straining and ACOM TEM: A novel method for analysis of plastic deformation of nanocrystalline metals* (2013) Ultramicroscopy **128** 68-81 doi: 10.1016/j.ultramic.2012.12.019

[17] D. Viladot, M. Véron, M. Gemmi, F. Peiró, J. Portillo, S. Estradé, J. Mendoza, N. Llorca-Isern and S. Nicolopoulous, *Orientation and phase mapping in the transmission electron microscopeusing precession-assisted diffraction spot recognition: state-of-the-art results* (2013) J. Microsc. **252** (1) 23-34. Doi: 10.1111/jmi.12065

[18] E.F. Rauch & Véron, *Automated crystal orientation and phase mapping in TEM* (2014) Materials Characterization **98** 1-9. Doi: 10.1016/j.matchar.2014.08.010

[19] J. L. Rouviere, A. Beche, Y. Martin, T. Denneulin, D. Cooper, *Improved strain precision with high spatial resolution using nanobeam precession electron diffraction*, Appl. Phys. Lett. 103 (2013) 241913. Doi:10.1063/1.4829154

[20] M.P. Vigouroux, V. Delaye, N. Bernier, R. Cipro, D. Lafond, G. Audoit, T. Baron, J.L. Rouvière, M. Martin & F. Bertin, *Strain mapping at the nanoscale using precession electron diffraction in transmission electron microscope with off axis camera* (2014) Appl. Phys. Lett. **105**, 191906. Doi: 10.1063/1.4901435

[21] D. Cooper, N. Bernier & J.L. Rouvière, *Combining 2 nm spatial resolution and 0.02% precision for deformation mapping of semiconducting specimens in a transmission electron microscope* (2015) Nano Lett. **15**, 5289. Doi: 10.1021/acs.nanolett.5b01614

[22] D. Cooper, T. Denneulin, N. Bernier, A. Becher & J-L. Rouviere, *Strain mapping of semiconductor specimens with nm-scale resolution in a transmission electron microscope* (2016) Micron 80, pp145-165 doi: 10.1016/j.micron.2015.09.001

[23] A.S. Eggeman, R. Krakow and P.A. Midgley, *Scanning precession electron tomography for three-dimensional nano-scale orientation imaging and crystallographic analysis* (2015) Nat. Comms. **6** 7267. Doi: 10.1038/ncomms8267

[24] W.J. Schaff, P.J. Tasker, M.C. Foisy and L.F. Eastman, *Device applications of strained layer epitaxy* (1991) Semiconductors & Semimetals **33** 73-138

[25] C. Mahr, K.Müller-Caspary, T. Grieb, M. Schowalter, T. Mehrtens, F.F. Krause, D. Zillman and A. Rosenauer, *Theoretical study of precision and accuracy of strain analysis by nano-beam electron diffraction* (2015) Ultramicroscopy **158** 38-48

[26] Y. Liao & L.D. Marks, *Reduction of electron channeling in EDS using precession* (2013) Ultramicroscopy **126** 19-22. Doi: 10.1016/j.ultramic.2012.11.007

[27] Y. Liao & L. Marks, *On alignment for precession electron diffraction*, Ultramicroscopy, 117 (2012) 1-6. Doi: 10.1016/j.ultramic.2012.03.021

[28] C. Koch, *Aberration-compensated large-angle rocking-beam electron diffraction* (2011) Ultramicroscopy **111** pp828-840 doi: 10.1016/j.ultramic.2010.12.014

[29] C.S. Own, L.D. Marks and W. Sinkler, *Electron precession: A guide for implementation* (2005) Rev. Sci. Inst. **76** 033703 doi: 10.1063/1.1866612

[30] J.F. Nye, *Natural Focusing and Fine Structure of Light* (1999) IoP Publishing, London, UK.

[31] M.V. Berry and C. Upstill, *Catastrophe optics: Morphologies of caustics and their diffraction patterns* (1980) Ch.4 in Progress in Optics VXIII (Ed: E. Wolf), North-Holland

[32] A.R. Lupini, *The electron Ronchigram* (chapter 3) in *Scanning Transmission Electron Microscopy – Imaging & Analysis* (Eds. S.J. Pennycook & P.D. Nellist) (2011) Springer, Berlin. Doi: 10.1007/978-1-4419-7200-2

[33] The aberration function is defined as phase shift (units in radians) of the warped converging wave-front relative to a spherical reference wave centred to the point where the optic axis crosses the Gaussian imaging plane.

[34] Philips/FEI Documentation (1997) *CM300F Electronics Circuits*, Vol 1.

[35] R. Erni, M.D. Rossell, C. Kisielowski and U. Dahmen, *Atomic-resolution imaging with a sub-50-pm electron probe* (2009) Phys. Rev. Lett. **102** 096101 doi: 10.1103/PhysRevLett.102.096101

[36] J.M. Cowley, *Twenty forms of electron holography* (1992) Ultramicroscopy **41** 335-348

[37] J.C.H. Spence, *Convergent-beam nano-diffraction, in-line holography and coherent shadow imaging* (1992) Optik **92** (2) 57-68

[38] J.A. Lin & J.M. Cowley, *Calibration of the operating parameters for an HB5 STEM instrument* (1986) Ultramicroscopy **19** 31-42

[39] E.M. James and N.D. Browning, *Practical aspects of atomic resolution imaging and analysis in STEM* (1999) Ultramicroscopy **78** 125-139

[40] N. Dellby, O.L. Krivanek, P.D. Nellist, P.E. Batson & A.R. Lupini, *Progress in aberration-corrected scanning transmission electron microscopy* (2001) J. El. Microscopy **50** (3) 177-185

[41] O.L. Krivanek, P.D. Nellist, N. Dellby, M.F. Murfitt & Z. Szilagyi, *Towards sub-0.5Å electron beams* (2003) Ultramicroscopy **96** 229-237. Doi: 10.1016/S0304-3991(03)00090-1

[42] H. Sawada, T. Sannomiya, F. Hosokawa, T. Nakamichi, T. Kaneyama, T.Tomita, Y. Kondo, T. Tanaka, Y. Oshima, Y. Tanishiro & K. Takayanagi, *Measurement method of aberration from Ronchigram by autocorrelation function* (2008), Ultramicroscopy **108** 1467-1475. Doi: 10.1016/j.ultramic.2008.04.095

[43] A.R. Lupini, P. Wang, P.D. Nellist, A.I. Kirkland & S.J. Pennycook, *Aberration measurement using the Ronchigram contrast transfer function* (2010) Ultramicroscopy **110** 891-898. Doi: 10.1016/j.ultramic.2010.04.006

[44] P. Horowitz and W. Hill, *The art of electronics* (1989) Ch.7, Cambridge University Press, Cambridge

[45] A. S. Eggeman, J. S. Barnard and P. A. Midgley, *Aberration-corrected and energy-filtered precession electron diffraction*, Zeitschrift für Kristallographie, 228 (2013) 43-50, doi:10.1524/zkri.2013.1565

[46] C. S. Own, W. Sinkler, L. D. Marks, *Prospects for aberration corrected electron precession*, Ultramicroscopy, 107 (2007) 534-542. Doi: 10.1016/j.ultramic.2006.03.011

[47] www.harrisgeospatial.com/ProductsandSolutions/GeospatialProducts/IDL.aspx

Figure captions

Figure 1. Schematic of the focussed precessing probe geometry for SPED. Two azimuths (dark green and light green) are depicted with one diffracted beam (purple) illustrated that shows the diffraction condition is only met at one particular azimuth. The Beam Upper and Lower Deflectors (depicted as inductors) shift and tilt the beam above the sample, the Image Upper and Lower Deflectors de-rock the diffraction pattern below it. Principal imaging and conjugate diffraction planes are indicated, as well as the principal focal planes of the objective lens (OL). Lenses labelled are: condenser (Cond.), diffraction (Dif.), intermediate (Int.) and objective pre (Ob. Pre.) and post (Ob. Post) specimen lenses.

Figure 2. The ray diagram of the precessed electron probe at two (opposite and instant) azimuths on the precession cone. With the probe crossover (C) and pivot point plane (P) at different heights to the sample (S), the shadow image inside the BF-CBED disk follows a circular path (thin dashed line inside CBED disk), of which opposite instantaneous azimuths are depicted in (a) & (b). However, in (b) the pivot point error has been reduced and the sample within the shadow image now follows a smaller circular path than before. Only when the pivot point error is zero (c), i.e. the pivot point plane (P) is coincident with the specimen (S), does the shadow image remain stationary within the BF disk. Finally, the probe crossover (C) is made coincident with the pivot point (by weakening the condenser lens) and BF disk appears featureless (d).

Figure 3. The steps involved in aligning the precessing probe are illustrated through time averaged images of the BF-CBED disk, with an integration time longer than one precession cycle, such that motion of the BF disk or of the shadow image within the BF disk appears as a blurring. The alignment begins by focusing the probe onto the sample and switching to diffraction mode. Overfocusing the probe with the condenser lens widens the BF CBED disk to give a large field of view (step 1). With precession on (step 2), de-rocking is adjusted first (Image Upper and Image Lower deflectors, Figure 1) to sharpen the BF disk (step 3). Next, the pivot point is adjusted (Beam Upper and Beam Lower deflectors, Figure 1) to give a sharp sample image within the BF-disk (step 4). As the overfocus is

reduced (step 5), the de-rocking and pivot points are refined (steps 3 & 4, repeated). When no further improvement can be achieved by pivot-point adjustment, the dynamic compensation is adjusted (step 6). The alignment terminates by refocusing and reducing the illumination aperture (step 7). The inset (*) shows the non-precessed shadow image at step 6 for comparison.

Figure 4. Virtual bright-field images of the gold-on-carbon test sample with a virtual collection angle of $\beta = 1.2$ mrad and their log-power spectra, $\log_{10}\rho(\mathrm{k}|\phi)$. Each VBF has 256^2 pixels, with width 1.9 nm. Nyquist frequency is 0.26 nm^{-1}.

Figure 5. Log-power-spectrum-ratios for small, medium and large precession angles (a). The dotted lines are the 2-parameter fits to the low$-k$ domain assuming a parabolic variation. The rises in the LPSRs for $k > 0.1$ nm^{-1} ($\phi = 33.7$ mrad), $k > 0.15$ nm^{-1} ($\phi = 13.5$ mrad) and $k > 0.2$ nm^{-1} ($\phi = 1.4$ mrad) correspond to the differing extents of the frequency-independent noise floors in each case. The precession-induced blur is shown in (b). The low$-\phi$ domain shows a $\phi^{0.4}$ variation for both 1- and 2-parameter fits; the high$-\phi$ domain show $\phi^{1.6}$ (2-parameter) and $\phi^{1.7}$ (1-parameter) variation. The probe size predicted by Vincent & Midgley is shown as a dotted line.

Figure 6. The geometric rays and wave-optical simulations of the electron probe for a convergent probe, tilted by a precession angle of $\phi = 35$ mrad, in the presence of spherical aberration coefficient ($C_{30} = 1.2$ mm) relative to the optic axis ($- - -$). The principal (central) ray crosses the optic axis at $C_{30}\phi^2$ and rays about this ($\phi \pm \alpha$) in the radial direction cross at $C_{30}(\phi \pm \alpha)^2$, creating two caustic folds in the probe – a radial caustic (line focus, X-direction) at $C_{30}\phi^2$ and an azimuthal caustic (Y-direction) at $3C_{30}\phi^2$ (Note: Lateral displacements between the wave-optical probe simulations have been removed for convenience). Halfway between these two folds, at a height of $2C_{30}\phi^2$, the probe is most compact. The Vincent-Midgley disk-of-least-confusion diameters are 5.9 and 17.6 nm for $\alpha = 1$ and $\alpha = 3$ mrad respectively.

Figure A1. Four simulated probes for one (instantaneous) azimuth with a precession angle of 35 mrad with illumination angles below, at, above and many times greater than the optimum illumination angle (a). The cumulative radially averaged electron probe as a function of shows the linear increase in probe size with illumination angle with 50% (red) and 80% (green) asymptotes illustrated (b).

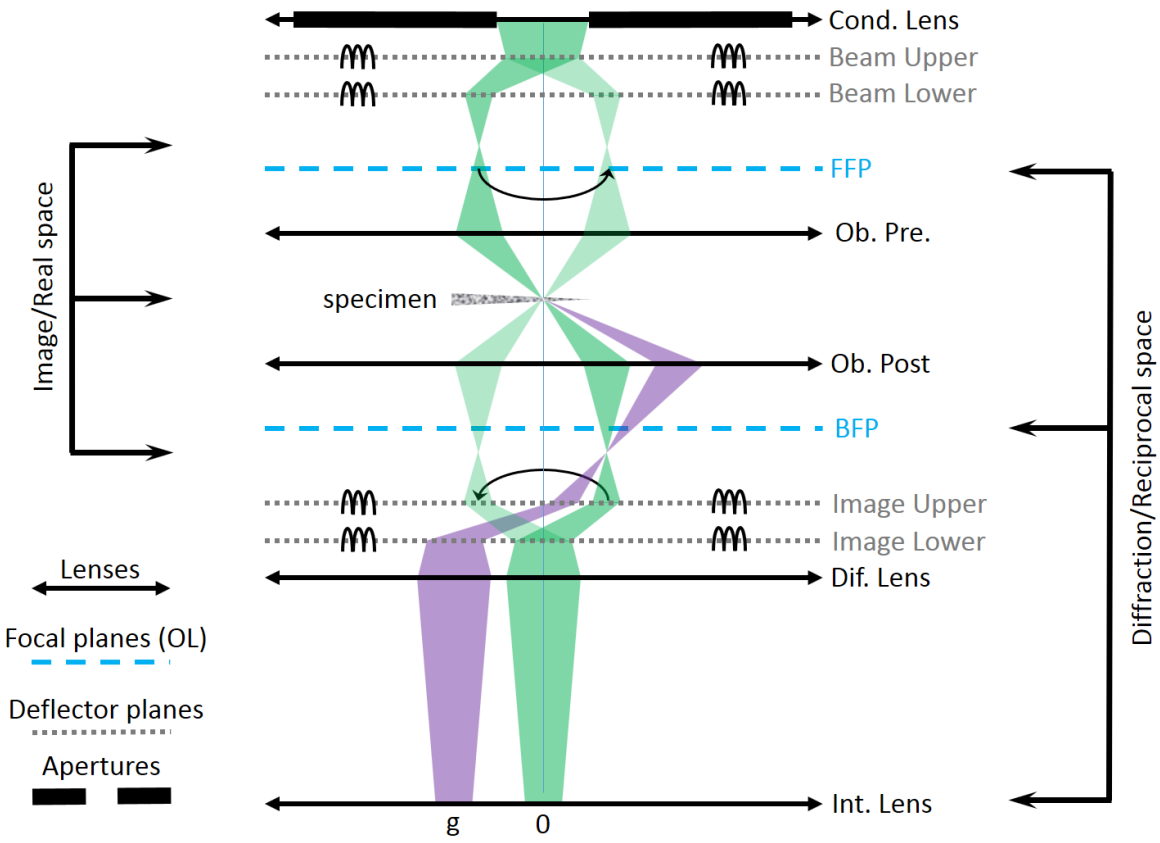

Figure 1

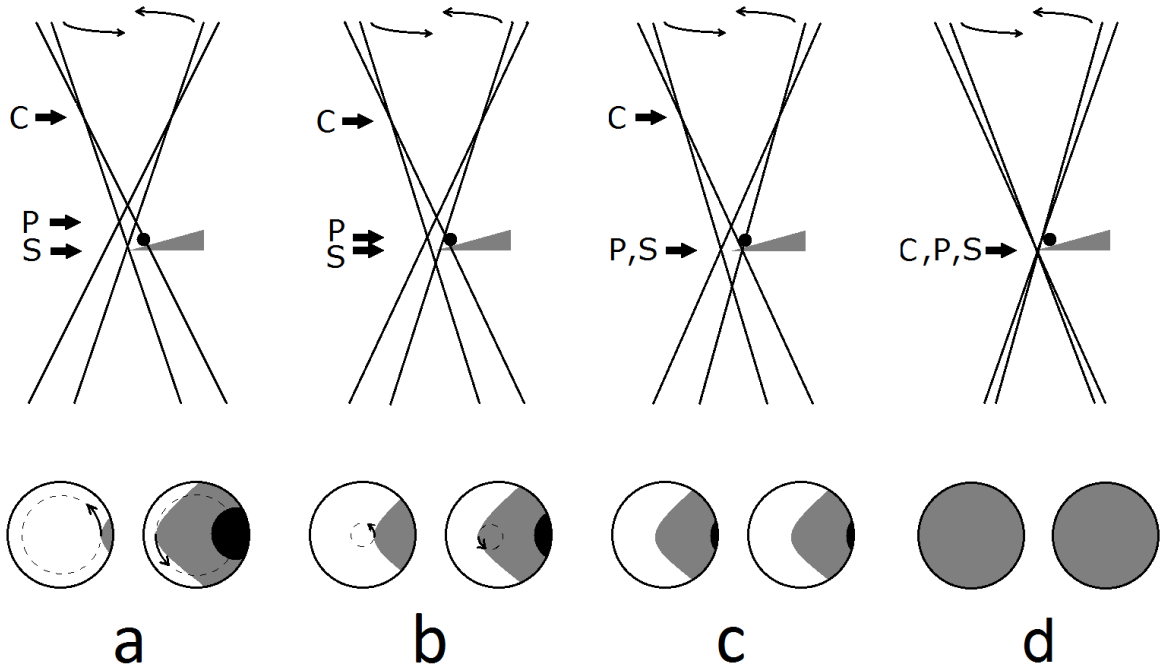

Figure 2

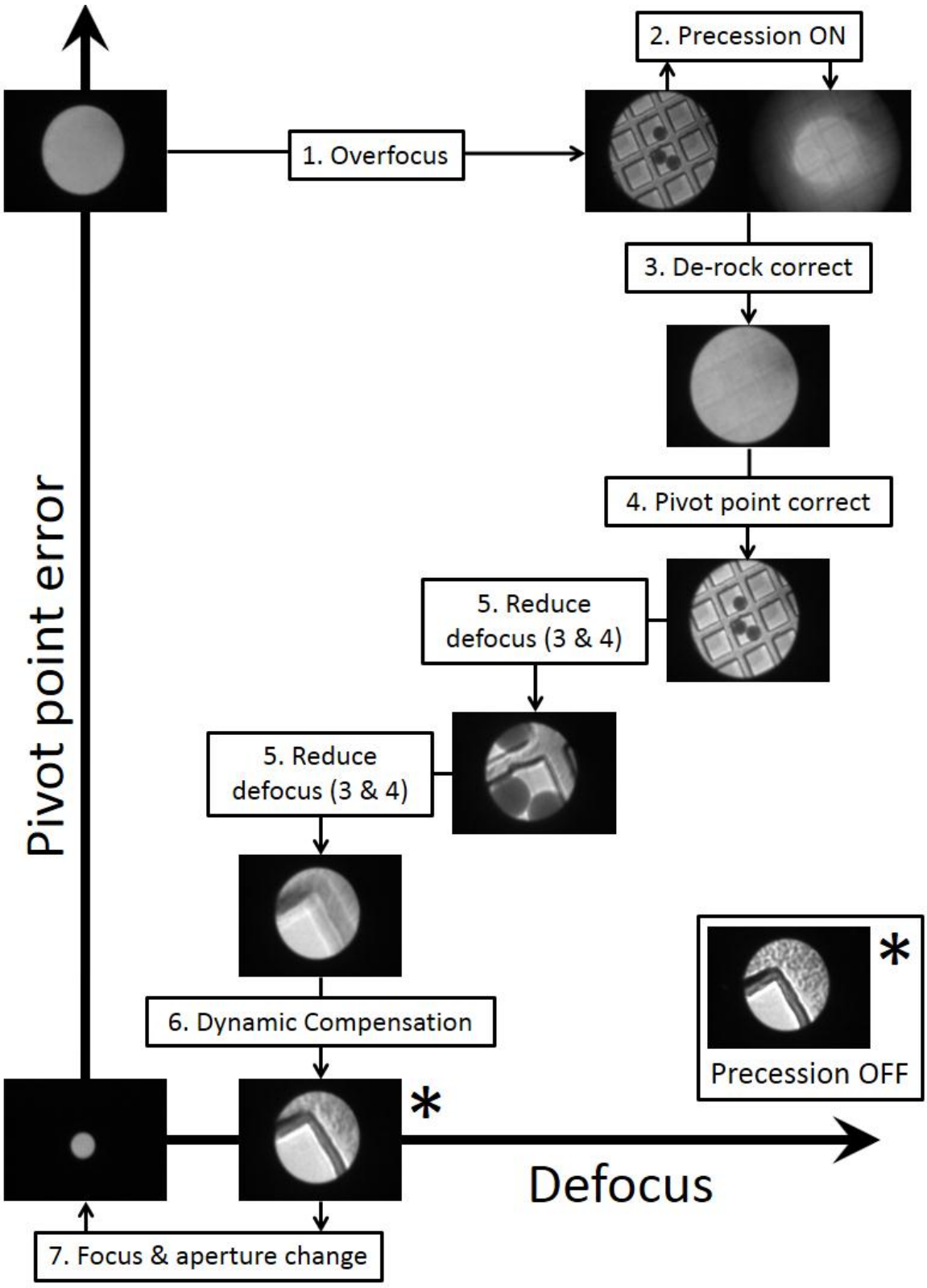

Figure 3

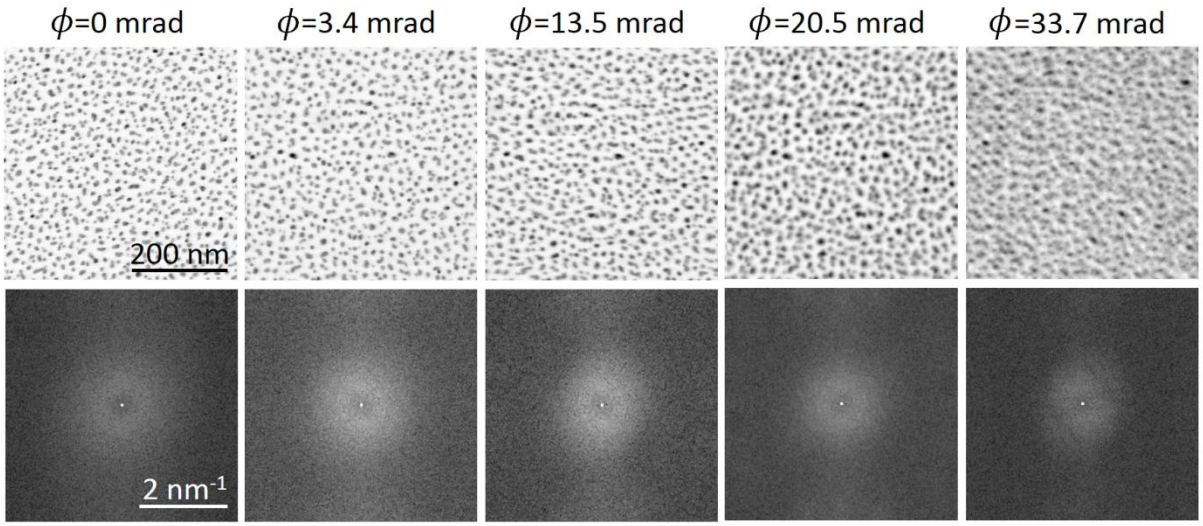

Figure 4

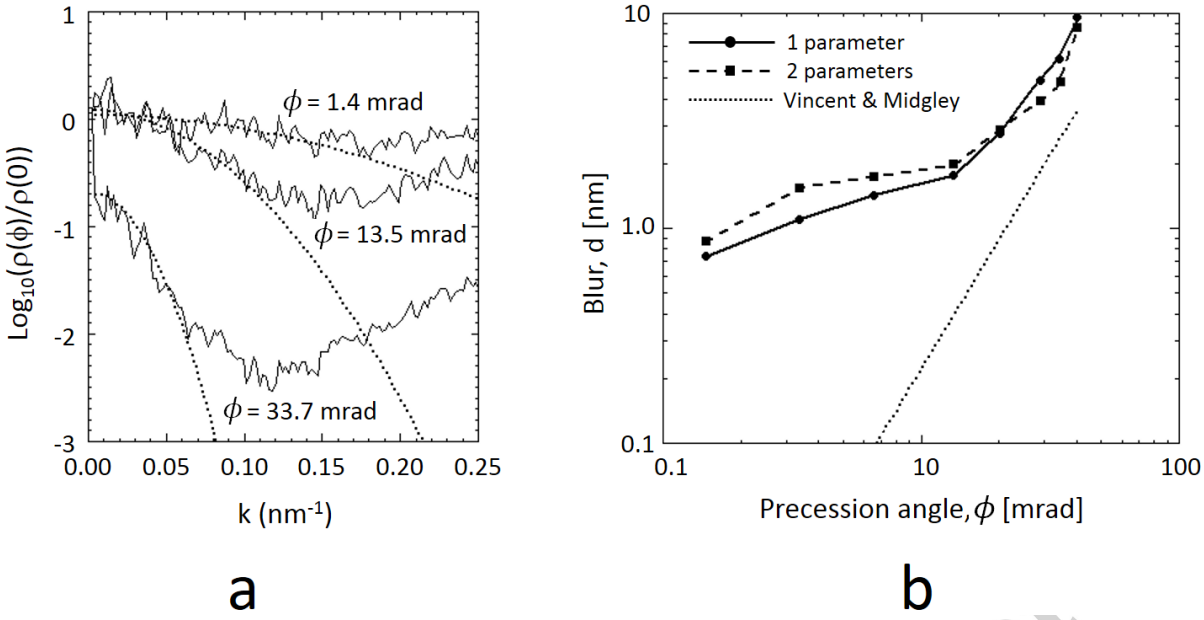

a b

Figure 5

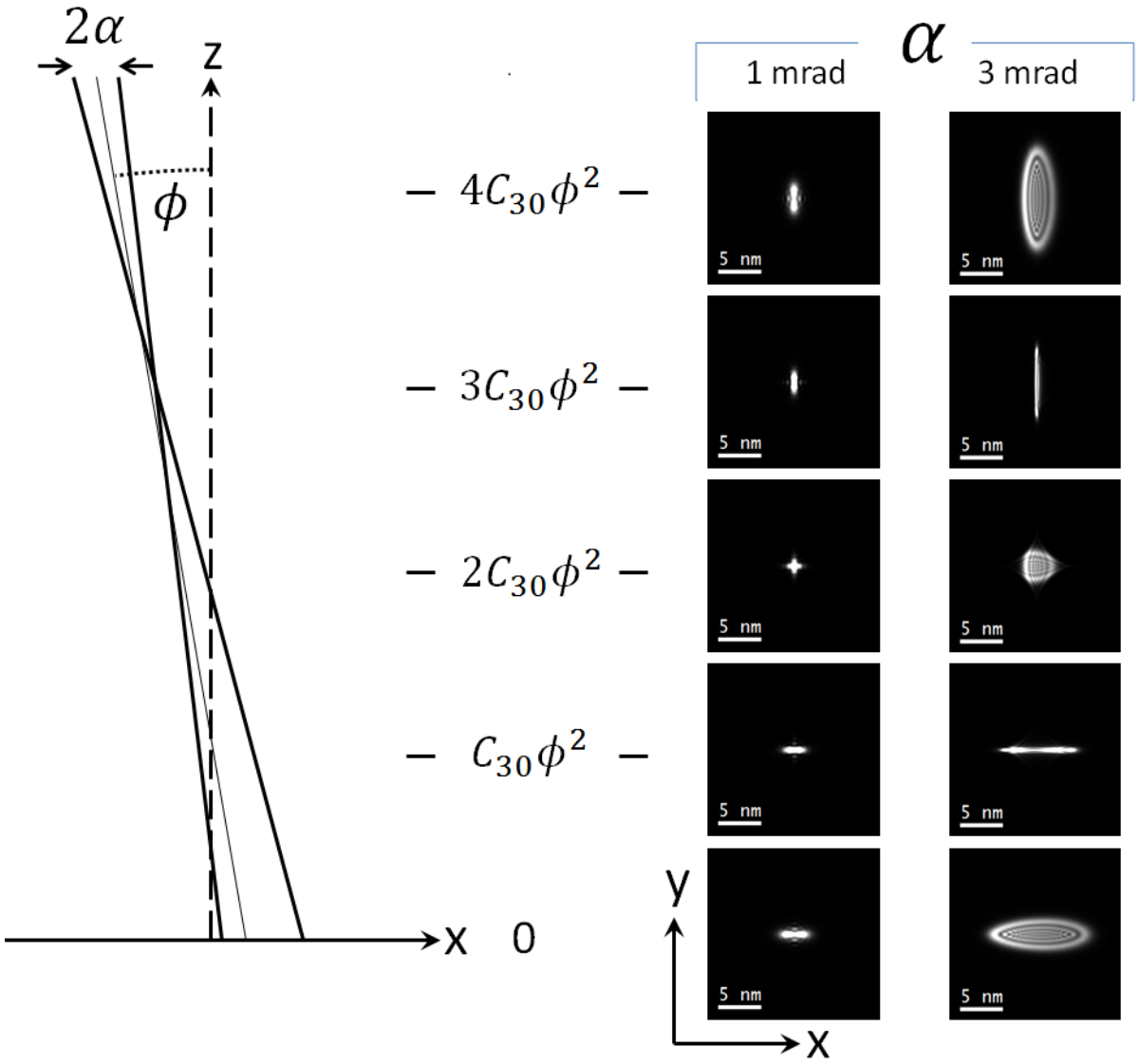

Figure 6

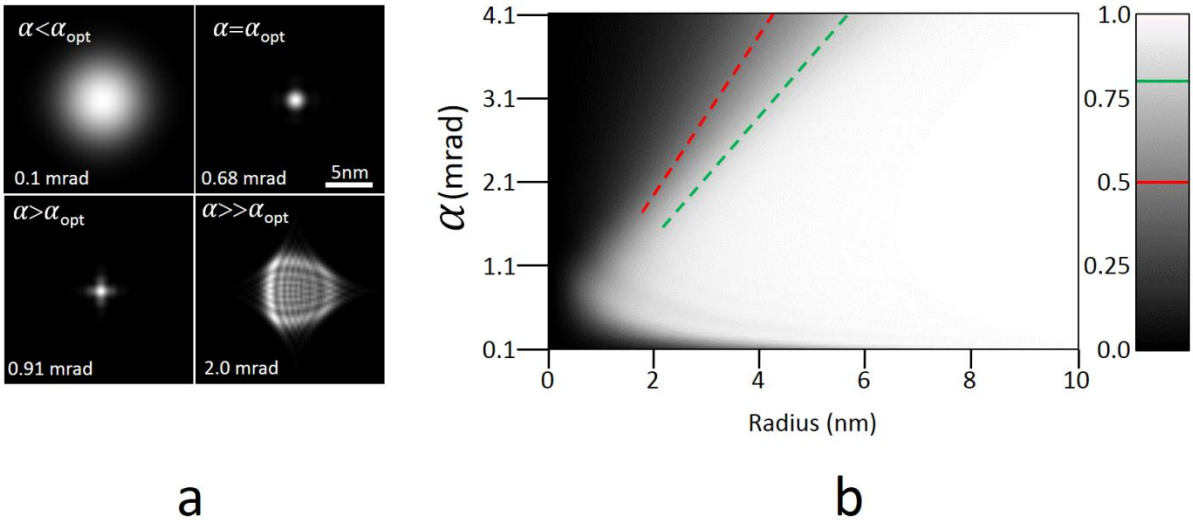

Figure A1

Highlights:

"High-resolution scanning precession electron diffraction: alignment and spatial resolution" by J. S. Barnard, D. N. Johnstone, and P. A. Midgley.

- A method for aligning the pivot point of a precessing electron probe is proposed.

- Assessment of the blur induced by precession in a scanned image is demonstrated.

- Physical limits governing the minimal size of a precessing electron probe are expounded.